Short-term memory errors are strongly associated with a drift in neural activity in the posterior parietal cortex

Joon Ho Choi[1,¶,*], Sungwon Bae[1,2,¶], Jiho Park[3], Minsu Yoo[1,3], Chul-Hoon Kim[2], L. Ian Schmitt[4], Ji-Woong Choi[3], and Jong-Cheol Rah[1, 5,*]

[1]Sensory and Motor Systems Neuroscience Group, Korea Brain Research Institute, 61 Cheomdan-ro, Dong-Gu, Daegu, 41062, Korea [2]Department of Pharmacology, College of Medicine, Yonsei University, 50 Yonsei-ro, Seodaemun-Gu, Seoul, 03722, Korea [3]Department of Electrical Engineering and Computer Science, Daegu Gyeongbuk Institute of Science and Technology (DGIST), 333 Techno Jungang-daero, Dalseong-gun, Daegu, 42988, Korea [4]Center for Brain Science, RIKEN, Wako, Saitama, Japan. [5]Department of Brain Sciences, DGIST, Daegu, 42988, Korea

[¶] These authors contributed equally

*Corresponding authors:

Joon Ho Choi

Sensory and Motor Systems Neuroscience Group, Korea Brain Research Institute, 61 Cheomdan-ro, Dong-Gu, Daegu 41062, Korea

joonchoi@kbri.re.kr

Jong-Cheol Rah

Sensory and Motor Systems Neuroscience Group, Korea Brain Research Institute, 61 Cheomdan-ro, Dong-Gu, Daegu 41062, Korea

jcrah@kbri.re.kr

Abstract

Understanding the neural mechanisms behind short-term memory (STM) errors is crucial for unraveling cognitive processes and addressing related deficits in neuropsychiatric disorders. This study investigates whether STM errors result from misrepresentation of sensory information or a decay in these representations over time. Utilizing 2-photon calcium imaging in the posterior parietal cortex (PPC) of mice engaged in a delayed match-to-sample task, we identified a subset of PPC neurons exhibiting both directional and temporal selectivity. Contrary to the idea that STM errors primarily stem from mis-encoding during the sample phase, our findings indicate that these errors are more closely associated with a drift in neural activity during the delay period. This drift results in a gradual shift away from the correct representation, ultimately leading to incorrect behavioral responses. These results emphasize the importance of maintaining stable neural representations in the PPC for accurate STM. Our findings also suggest that targeting PPC activity stabilization during delay periods could be a potential therapeutic strategy for mitigating cognitive impairments in disorders like schizophrenia.

Keywords:

Short-term memory, posterior parietal cortex, 2-photon calcium imaging, error trials, neural activity

Introduction

Short-term memory (STM) is a capacity to retain immediately relevant information over a brief period, typically on the order of seconds to minutes. While STM plays a pivotal role in a multitude of cognitive functions, representations in this system are fragile and prone to errors in information retention leading to sub-optimal behavior. Despite their behavioral impact, there is currently no circuit-level understanding of how STM errors occur due to a lack of systematic investigation. Gaining insight into the circuit mechanisms underlying STM errors is crucial for comprehending information retention and its relevance to various psychiatric disorders, including schizophrenia and attention deficit hyperactivity disorder, which frequently manifest deficits in STM[1–3] This study aims to examine the circuit underpinnings of STM errors. To this end, we considered two potential mechanisms which may underlie error generation: (1) Inadequately encoding of information in the neural activity, and (2) Disruption of encoded information during the delay period.

Along with the prefrontal cortex (PFC), the posterior parietal cortex (PPC) is a critical brain region responsible for maintaining information during STM[4–6]. We chose to elucidate the activity of the PPC for several reasons. As a major multimodal association cortex, the PPC is ideally positioned to integrate multimodal sensory information and relay this accumulated information to prefrontal areas[6,7]. Thus, if inadequate evidence accumulation or misperception were represented in both the PFC and PPC during error trials, the PPC is more likely the source of the erroneous activity that leads to the representation error. Furthermore, in both primates and rodents, a subset of PPC neurons exhibits direction-predictive firing rate changes in a graded

manner, reflecting the clarity of evidence during a decision-making task such as the random dot motion discrimination task or Poisson click task[8,9]. Meanwhile, neurons in the prefrontal motor area demonstrate more categorized activity changes, suggesting that the cumulative evidence information in the PPC transformed into a discrete decision in the PFC. Therefore, we hypothesized that the gradual degradation of encoded information could be more readily observed in the PPC compared with the PFC. By focusing on the PPC, we aimed to capture these subtle variations in sensory encoding and retention.

Despite extensive evidence implicating the PPC as a substrate for STM, the nature of information maintenance in this circuit remains incompletely understood. In a previous study, mice were trained to navigate through a virtual T-maze by choosing a left or right turn according to visual cues presented while PPC activity was measured. Since the cue was presented only in the first half of each trial, the mice had to rely on their STM to perform this task. This study revealed that the PPC exhibits a complex population encoding characterized by direction- and phase-selective sequences of activity across multiple neurons[6]. However, given that PPC activity shows navigational attributes, the PPC activity during the task cannot be interpreted as simply reflecting visual STM[10–12]. Indeed, Krumin and colleagues have illustrated that sequential PPC activity can be accurately predicted by the combination of heading direction and spatial location within the virtual corridor during a comparable behavioral task[13]. Task-relevant increases or suppressions in PPC activity have also been observed in mice performing a visually guided delayed go/no-go task[6,14]. Notably, 'go' signals exhibited selectivity and were represented by a substantial number of neurons, while 'no-go' signals were represented relatively weakly[6,14],

raising questions about whether the activities genuinely represented the retained visual signal itself, or rather pertained to the suppression and release of impulsive movement[15].

To more directly investigate how retained sensory information during the delay period may be encoded in PPC activity, and how it may be disrupted in errors, we recorded PPC activity while mice performed a delayed match-to-sample task that did not require navigation. A large fraction of the imaged neurons in PPC showed activity that reflected memory-guided decision-making, and the activity pattern of neurons in this population were remarkably similar to those identified in previous STM studies[6] consistent with a common mechanism of encoding for short-term representations across tasks. Comparison of PPC activity between correct and incorrect trials in this task revealed that STM errors were associated with weak initial encoding of the signal followed by spontaneous drift towards incorrect representation during the delay. These findings elucidate the circuit mechanisms underpinning errors in STM, providing insight into the nature of this function and opening future avenues to study how it might be disrupted in neuropsychiatric disorders.

Results

A sequence of choice-dependent neuronal activity in PPC

Our aim is to determine the extent to which PPC activity plays a pivotal role in maintaining sensory information within the context of a STM-dependent perceptual decision-making task, with an exclusion of spatial location and head-direction involvement. To achieve this, we trained seven transgenic mice expressing GCaMP6f (C57BL/6J-Tg(Thy1-GCaMP6f)GP5.5Dkim/J) to perform STM tasks. In brief, the mice were head-restrained, and gratings were presented on a screen in front of them, moving either to the left or right direction in a pseudo-random manner. Following around 2-second delay in which visual stimulation was omitted, a bifurcated lick port was presented within the reach of the mice. Correct responses, licking the corresponding lick port, were rewarded with approximately 5 μl of tap water, while incorrect responses, licking the wrong lick port, led to an extended inter-trial interval of 2 seconds (time-out) (see Fig. 1A). After thorough training, the mice successfully learned this task, achieving a discrimination rate exceeding 70%. Importantly, mice did not exhibit a bias towards either direction after training (Fig. 1B-C).

During task performance, we recorded the activities of PPC neurons by analyzing the fluorescence changes in the GCaMP6f-expressing layer (L) 2/3 neurons with two-photon laser scanning microscopy. The identification of the PPC region was based on stereotaxic coordinates derived from mesoscopic connectivity analysis, which revealed distinct antero- and retrograde connections compared to neighboring areas[16]. Active neurons were identified through *post hoc* analysis using the CaImAn software[17]. While various types of responses were observed from the

PPC neurons, a large proportion of neurons consistently exhibited selectivity based on direction, task phase, or both across trials (Fig. 1D). In addition to the remarkable response consistency across trials, the time-wise correlation of mean response vectors, computed every 0.5s (15 image frames) across all recorded neurons, demonstrated similarity within behavioral phases (Fig. 1E, see Methods).

To objectively categorize active neurons based on their response patterns, we employed a modified generalized linear model (GLM), as detailed in the Methods section[18]. The time-correlation of the activity vectors from the neurons sorted by our GLM was nearly identical to those from all the recorded neurons (Supplementary Fig. 1). This suggests that the phase-dependent feature of the activity is well preserved in the GLM-sorted neurons. Our analysis revealed that nearly half of the active neurons in the PPC satisfied the criteria for phase or stimulus direction selectivity ($p < 0.01$), amounting to 2,664 out of 4,569 neurons (Supplementary Fig. 2). Approximately 60% of these neurons (1,609/2,664 neurons, 873 for the right signal and 736 for the left signal) exhibited directional selectivity, the remaining neurons responded similarly to both directions (Supplementary Fig. 3A-C). Out of the 1,609 directionally selective neurons, approximately 41% displayed phase selectivity, with 661 neurons exhibiting phase selectivity during the sample phase, 315 during the delay phase. Consistent with previous studies, PPC neurons rarely displayed sustained activity across multiple phases of the task [6] (Fig. 1F and Supplementary Fig. 4) with less than 8% (202/2664) of neurons demonstrating phase selectivity during both the sample and delay phases.

When the neurons were sorted based on the onset of the peak responses, it became evident that a directional-selective sequence of neuronal activity emerged with a remarkable similarity to the findings of Harvey and colleagues [6] (Fig. 2A). This result underscores the replicability of the directional-selective sequence of neural activity in the PPC within a behavioral paradigm that excluded spatial navigation. To assess predictive capabilities of the GLM-selected neurons, the direction selectivity of each neuron was verified through receiver operating characteristics (ROC) analysis (Fig. 2C-D). It is noteworthy that while ROC analysis identifies neurons with significant differences in condition-dependent ΔF/F amplitude, modified GLM analysis detects neurons based on condition-dependent response selectivity. We introduced a preference metric, preference index (PI), which was proportional to the hyperbolic area of the ROC curve, calculated as (AUC-0.5)*2. The preference index of the neurons with temporal and directional selectivity was significantly higher compared to the shuffled responses, particularly for the delay-preferring neurons (Fig. 2C, D). It was noteworthy that over 30% of the phase- and direction-selective neurons exhibited a preference index above 0.9, indicating a near-complete separation in their responses to the two visual stimuli (Fig. 2B-C). Because PI was calculated based on the averaged responses[19], we also sought to quantify the consistency of the responses across trials. To this end, we constructed a reliability index (RI) proportional to the hyperbolic area of the area under ROC curve from the ΔF/F of all trials (see methods). Similar to the PI, a significantly high RI was observed in the direction-selective neurons compared to the shuffled control or non-directional neurons (Supplementary Fig. 3). Interestingly, direction-selective delay neurons showed a greater RI than sample neurons, suggesting refinement of the encoded information following stimulus-offset (Supplementary Fig. 3D-I).

Phase-selective activities were further validated across the population by using principal components analysis (PCA) to captures the temporal activity pattern of each neuron throughout the entire behavioral session (Fig. 2E). The GLM-identified phase-selective neurons (dots with corresponding colors) form distinct populations in the principal component space, demonstrating that our modified GLM algorithm accurately identifies neurons with phase-specific firing patterns.

To determine if the activity patterns we observed were organized anatomically, we further assessed the relative co-localization of PPC neurons with similar response properties. Specifically, we compared the distance within groups of neurons with shared functional characteristics to the distance across groups (Supplementary Fig. 5). Consistent with previous results for STM activity in navigation tasks[6], we found that the distances to functionally similar neurons were not significantly different from the distances to neurons with distinct firing patterns, refuting the hypothesis that activity patterns were specifically localized.

In summary, our results support the view that activity sequences in the PPC can encode short-term memory of sensory input, even in a delayed match-to-sample task that does not require encoding of heading direction or spatial location.

Functional characteristics of directional neurons in error trials

Having established that the PPC neurons exhibit direction- and phase- selectivity without the involvement of spatial navigation, we next sought to discern the mechanisms by which PPC activity may be disrupted on error trials. Specifically, we aimed to determine whether

inadequately encoded sensory inputs during the sample phase, poor retention of the encoded sensory information during the delay phase, or both, could reflect disrupted STM in error trials.

The activity of selective PPC neurons identified in correct trials showed markedly lower phase- or direction-selectivity on error trials (Fig. 3A). At the level of individual neurons, we often observed that neurons with high PI exhibited opposite directional selectivity, on error trials (Fig. 3B). It is important to note that not all the directionally selective neurons responded in the opposite direction, suggesting a mixed population response but one in which there is some degree of mis-encoding of the STM. There was a significant reduction in the PI during incorrect trials, particularly among the neurons that had a high PI in correct trials (Fig. 3C). In fact, the magnitude of reduction in PI was greater for the neurons that had a high PI in correct trials (Fig. 3D and Supplementary Fig. 6). The median ΔPI for the neurons with an initial PI between 0.9 and 1 was approximately -1, suggesting that nearly half of the highly reliable neurons lost response-selectivity or responded to the opposite direction during error trials. To assess how activity changes were related to the consistency of responses on individual trials, we also examined the trial accuracy-dependent difference in RI value for each phase- and direction-selective neuron as well as non-direction selective neurons (Fig. 4A-I and Supplementary Fig. 6). This analysis revealed that a greater proportion of sample-phase neurons hold directional information regardless of trial accuracy, while delay neurons exhibited greater activation in the opposite direction during error trials. Notably, highly reliable directional delay neurons showed the greatest reduction in the PI and RI in error trials (Fig. 4 B-I). Together, these results indicate that directional delay neurons with high reliability are likely to show a response pattern opposite to their responses on correct trials.

A reversal of the response firing for neurons with high PI would predict that the overall difference between preferred and non-preferred directions would be diminished. Indeed, we found a significant reduction in the difference between the ΔF/F of preferred and opposite directional cues for error trials (Fig. 4J). This reduced difference was more pronounced for the delay-selective neurons. We observed a reduction in ΔF/F in the preferred direction and an increase in ΔF/F in the opposite direction, rendering the two responses during the delay period indistinguishable (Fig. 4K). This suggests that the response selectivity of delay neurons was more affected than that of sample neurons in error trials.

Activity trajectory distances of the direction-selective PPC neurons during the task

The observation that a fraction of the direction-selective neurons showed activity patterns corresponding to their response to the opposite directional signal during error trials is potentially consistent with either mis-encoding or disrupted retention of STM information. To more directly compare the relative contributions of these two possible mechanisms, we next examined the temporal changes in the population-wide activity of directional neurons. Specifically, we sought to determine if the STM associated population dynamics initially resembled the opposite direction during the sample phase, if it gradually became more like the opposite direction as the trials proceeded, or both.

To this end, we first captured the dynamics of direction-selective neurons in a reduced dimension as a trajectory through activity space using PCA. The activity trajectories from the correct preferred direction responses of direction-selective neurons (specifically, the left trial responses

of left-preferring neurons and the right trial responses of right-preferring neurons) were designated as preferred directional correct responses or PP. Conversely, the trajectories from the correct opposite-directional responses (i.e., the right trial responses of left-preferring neurons and the left trial responses of right-preferring neurons) were dubbed opposite directional responses or OO. (Fig. 5 and Supplementary Fig. 8). We next calculated the distance between these trajectories as a metric of the activity difference across conditions (Fig. 5A). The trajectory distance between PP and OO (d1) remained stably high throughout the sample period and increased further during the delay period (Fig. 5C, d1). As a control, we also calculated the distance between randomly selected preferred trials and the remaining preferred trials to assess the magnitude of variability in activity (Fig. 5C, d0).

To assess the changes in the activity of direction-selective neurons during error trials, we compared the trajectory distances from error trials to both correct trials, PP and OO. During error trials where preferred directional inputs resulted in an opposite direction response (PO), such as left-preferred neuron activity in left stimuli-right response and right-preferred neuron activity in right stimuli-left response errors, the trajectory distance to the correct OO activity (Fig. 5D, d2) increased and more or less saturated around the first 0.5 seconds of the sample period. However, d2 in the sample phase saturated at a lower distance than d1, suggesting a relatively poor activity distinction by stimulus direction (two-tailed unpaired t-test; $n=100$, $p < 0.001$ Supplementary Fig. 8A). The d2 then decreased from the late sample phase through the delay period (gray area). Conversely, the trajectory distance between PO and PP (Fig. 5D, d3) decreased during the sample period yet remained significantly greater than d0 (two-tailed unpaired t-test; $n=100$, $p < 0.001$, Supplementary Fig. 8B). The d3 then increased dramatically during the delay phase.

Together, these results suggest that during the sample phase of PO errors, PPC neurons fired similarly to PP but with relatively poor distinction by stimulus direction. Over the late sample phase to the delay phase, the activity increasingly resembled the opposite directional firing. Similarly, the activity in error trials where opposite stimuli resulted in preferred directional responses (OP) showed decreasing distance to OO during the sample phase and drifted significantly during the delay phase (Fig. 5E, d4). The activity distance between OP and PP (d5) increased during the sample phase and showed a slight decrease at the end of the delay phase.

However, because the error activity trajectories are not necessarily located within the same activity plane as the PP and OO trajectories, a closer distance to PP does not guarantee a distant relationship to OO. To evaluate the relative distances in a multi-dimensional space, we devised a trajectory similarity index (TSI). The TSI measures the differences in distances to PP and OO, normalized by the sum of those distances, so that a higher absolute TSI indicates greater similarity. The polarity of the TSI value indicates whether the activity is more similar to PP (positive) or to OO (negative) (illustration in Supplementary Fig. 8C, see Methods for details). In line with the analysis of distances to the PP or OO activity (d2-d5), the TSI during the sample phase showed weak yet significant directional activity according to the given stimuli. However, as the delay progressed, the activity drifted toward the opposite direction (Fig. 5F).

Population activity of PPC neurons during the task

The activity trajectories in the principal component dimension were computed using the combined activities of direction-selective neurons across sessions. To understand how these dynamics might relate to the overall population activity, we next employed measures that assess

activity across all recorded neurons. Specifically, we applied linear discriminant analysis (LDA) to compare population activity during error trials with that observed in correct trials, where the stimulus direction was either the same or opposite. This approach provided a measure of the signal-to-noise ratio (SNR) of the encoded signal across the population, where the signal denotes the distance between the two responses in the activity space, and the noise reflects the variance within the responses (see Methods). We measured the SNR changes of error trials within a moving window of 50 frames in the hyperplane that best discriminates between correct left- and right-trials (Fig. 6). Consistent with the trajectory distances of direction-selective neurons, the SNR between correct and same-stimuli error trials (correct left trials (LL) vs. Left stimulus-Right (LR) response and correct right trials (RR) vs. Right stimulus-Left response (RL)) initially decreased, reaching saturation around the middle of the sample period (approximately 30 frames). As the frames from the delay period were included (after the 70th frame), the SNR increased (Fig. 6A, left). On the other hand, the SNR between correct and incorrect trials with the opposite stimuli (same response error, LL vs. RL and RR vs. LR) exhibited an opposite pattern: an initial increase and saturation over 30 frames during the sample period, followed by a subsequent decrease during the delay period (Fig. 6A, right). The patterns of same-stimuli and same-response errors aligned with the TSI changes in OP and PO errors, respectively (Fig. 5F). While the grouping of 50 frames across trials ensures the separation between groups, this analysis obscures the SNR changes during the delay period. To better visualize the SNR changes during the delay period, we replotted the measured SNR for categorizing every 30 frames of all trials within the delay period (Fig. 6B). While the same signal errors became more differentiated during the delay period, a decreasing SNR was observed in the same response errors. Across all frames, during same-stimuli errors, PPC activities were relatively similar in the sample phase but

diverged more significantly during the delay phase. In contrast, in same-response errors, the activity differences driven by stimulus direction in the sample phase diminished during the delay phase (Fig. 6C). These results highlight the role of activity drift toward the opposite direction in contributing to the erroneous STM.

While our analysis using PCA and LDA revealed that the activity difference in error trials compared to correct trials, the observed activity difference may not directly reflect a representation of the directional content of sensory inputs. To address this issue, we employed a dimensionality reduction approach to identify population activity modes that distinguish features of interest, particularly the signal corresponding to the direction of motion in the visual stimulus (coding direction or CD). To directly compare signal direction-dependent activity modes, we computed projections along a vector in the activity space of all recorded PPC neurons that maximally differentiate sensory direction in the sample (CD_{sample}) and delay phase (CD_{delay}) (Fig. 6D). To compare the separation of the direction signals, we projected the error trial activities onto the vector. In comparison to correct trials, the directional sensory signals were weaker and less distinguishable between directions, particularly during the delay phase of error trials (Fig. 6D-E).

Consequently, we aimed to assess how accurately correct or error trials could be predicted. We trained a Support Vector Machine (SVM) model using the activities of PPC neurons during correct trials. Subsequently, we evaluated the accuracy of decoding sensory direction from the trial-by-trial population activity of PPC neurons using the SVM decoders. We labeled PPC activity from randomly chosen 70% of correct trials in a session as belonging to either the left or

right direction, and the remaining trials were used to test prediction accuracy (Fig. 6F). For correct trials, the prediction accuracy of the classifier significantly increased above the shuffled control level (grey line) at the onset of the sample phase and remained elevated until the end of the delay period. When assessing error trials using the same hyperplane generated from correct trials, the prediction accuracy showed a slight temporal delay but eventually reached a level comparable to that of correct trials. This result suggests that despite a significant reduction in the distinction between stimulus directions, the population activity of PPC neurons still encodes the correct direction. However, during the delay period of error trials, the prediction accuracy dropped rapidly, falling below chance level by the end, indicating a tendency toward choosing the opposite direction. Taken together, our results demonstrate that population activity in PPC, resembles the responses to the opposite directional signal in error trials especially during the delay phase, and thus that STM memory errors are associated with a reversal in the stimulus content encoding within PPC.

Discussion

Distinguished sensory information maintenance from navigational and movement signals in PPC activity during STM

In the current study, we observed propagating neural activity that tracked the sensory information being maintained during STM task performance. While similar observations have been made previously in STM-based virtual T-maze task[6] a subsequent study have raised questions about the interpretation of these findings, pointing out that the choice-dependent

activity sequence could be predicted by heading direction and the animal's position in the virtual corridor and so may reflect a navigational signal[13]. This view is consistent with earlier studies reporting PPC neurons exhibited activity changes due to locomotor actions, including turning and forward motion, when these motions were associated with spatial references[11,12,20,21]. Thus, distinguishing between the activity related to sensory information maintenance and that influenced by navigational context is crucial for a better understanding of the PPC function in STM. Sensory cue-dependent go/no-go tasks also have limitations due to possible alternative interpretations, such as preparatory activity of impulsive licking behavior and their suppression[6,14,19,22]. In our study, we re-examined PPC activity during an STM task that required retaining visual information and making choices with an equivalent directional licking behavior without a spatial component. Despite this, we found remarkably similar activity in PPC neurons. We observed direction-selective activity sequences that predicted sensory direction in the PPC not only in the absence of navigation but also without ongoing stimulus during the delay period. Moreover, the disruptions of activity patterns associated with error trials were consistent with a drift towards an erroneous representation of stimulus direction, further supporting the view that the observed activity reflects an STM signal.

Difference in population activity in error trials

A sizeable proportion of the PPC neurons exhibited significant directional preferences, with over 30% showing exceptionally high selectivity (PI> 0.9, Fig. 2A-C). The majority of the direction selective neurons were tuned to either of the phases simultaneously, rather than exhibiting sustained activity throughout both periods (Fig. 2A and D). Highly reliable directional firing or

high PI could be ensured by the wiring motif observed in the PPC, where co-selective neurons have strong and more frequent synaptic connections while inhibiting anti-selective neurons[23].

In the PCA-driven activity subspace, which captured over 70 % of the selective neurons' activity (Supplementary Fig. 8), trajectories driven by the two-directional visual stimuli were differentiated immediately after the stimuli onset and continued to diverge during the delay period (Fig. 5C and 6B). It was rather unexpected that the activity trajectories were further differentiated during the delay period in the absence of sensory stimuli. This phenomenon was also consistent with the significantly greater direction-selectivity of the delay neurons compared to sample neurons (Fig. 2D). These findings support the hypothesis that the primary function of the PPC is to maintain the differentiated sensory inputs collected during the sample period, rather than to detect and encode this signal. This latter function may instead depend on early processing within sensory cortical areas[6,14,24]. The continuous increase in activity differences during the delay phase may reflect the processing time required to optimize the acquired visual information and minimize activity variability, occurring in parallel with the time needed for premotor neurons to prepare and execute invariant motor responses[25,26]. These possibilities could be distinguished through a systematic comparison of PPC activities with varying stimulus length and complexity.

Our various, complementary multivariate population analyses consistently demonstrated a retention of differences in population activity in response to different stimuli in correct trials (Fig. 5C, and 6F). Although the underlying population activity is spread across multiple neurons, this encoding pattern is nonetheless reminiscent of the increased (or decreased) and sustained

firing rate in PPC neurons of primates[8,27] or rats performing tasks that require STM[9]. Hence, it is tempting to propose that the population activity difference in mouse PPC is analogous to the quality of evidence. In this scenario, differences in PPC activity between cue directions that develop during the sample period would serve as the basis for stimulus encoding, while the maintenance of these differences over the delay period would correspond to retention of this information. Consistent with this idea, we observed weaker directional differentiation and poor maintenance of differences in PPC activities during error trials. These observations suggest that STM errors are associated with weaker encoding of sensory information and a progressive weakening of this information throughout the STM task (Fig. 5-6). However, it is noteworthy that despite the 'misunderstanding' of some neurons and the resulting reduced activity distinction during the sample phase of error trials, population-level activity in the PPC still sufficiently encodes the correct direction (Fig. 6F).

Increasing opposite directional activity of PPC neurons in error trials

While the origin of the reduced distance in activity space on error trials remains unclear, changes in the arousal state of the animal may account for this poor encoding. The level of arousal varies continuously and neuronal responses in sensory cortices as well as high-order cortical areas including PPC are critically modulated by attentional states[6,28–33]. In error trials with insufficient arousal, the activity of PPC neurons in response to the preferred visual stimuli would decrease, leading to relatively poor separation in the activity space (Fig. 3D and 4G-H). However, neurons with negative PI values, which exhibit greater firing to the opposite directional stimuli than the preferred direction, cannot be explained by this modulation. Instead, we believe that PPC activity encodes how the stimulus was 'understood' rather than the stimulus identity per se, particularly

for delay neurons and to a lesser degree for directional sample neurons (Fig. 3 and 4). Supporting this idea, neurons in the PPC of macaques showed firing changes that could predict behavioral choices even with 0% coherence in a random dot motion task[8].

Recent anatomical analysis has demonstrated that the probability and strength of the L2/3 PPC neurons are dependent on the similarity of directional selectivity[23]. Moreover, PPC subnetworks with opposite selectivity appear to suppress one another through mutual inhibitory connections[23,34,35]. Based on these findings and our results, we propose that direction-selective delay neurons form stronger subnetworks than sample neurons. In error trials, although the opposite-directional PPC activity during the sample phase does not initially alter the perceived direction of the stimuli, it may be amplified through tightly interconnected delay neurons, ultimately leading to an inversion in the encoded direction and resulting in an error. This idea is consistent with our findings, which illustrate a significantly greater PI and RI in delay neurons compared to sample neurons (Fig. 2D and 4), as well as the drifting of population activity toward the opposite direction as the delay progresses (Fig. 5F and 6).

Limitation of the study

Due to the limited number of task-relevant neurons recorded in a single trial, compounded by the intrinsic noise of cortical activities, we based much of our analyses on averaged activity across numerous trials of the STM task. As a result, it was not plausible to reliably track the onset and amplification of inappropriate directional firing in the current study, both the origin of erroneous activity within the subnetwork and the nature of its amplification remains unresolved. Further, even though the PPC activities were acquired while mice were engaged in head fixation to

perform the task, unintended movement or arousal state may occur that could modulate PPC activity [33,36]. It would be an intriguing avenue for future study to access trial variability with variable attentional conditions with the aid of high-density electrophysiological recordings[37–41].

Conclusion

In conclusion, our study sheds light on the neural mechanisms underlying sensory encoding and retention in STM tasks, emphasizing the role of the PPC in these processes. By elucidating the relationship between PPC activity patterns and task performance, we provide valuable insights into the cognitive functions of the PPC and with major implications for understanding STM errors. Since reduced STM performance is one of the key symptoms in schizophrenia[42–44] as well as an endophenotype of other neuropsychiatric disorders[45] insight into the nature of errors occur in STM also hold major translational relevance. Thus, our findings open new avenues for research aimed at developing novel therapeutic approaches for these disorders. Future research exploring trial variability and attentional conditions using advanced recording techniques will further enhance our understanding of PPC function in STM as well as how it may be disrupted in disease.

Declaration of generative AI and AI-assisted technologies in the writing process

During the preparation of this work the authors used ChatGPT-OpenAI in order to correct grammatical errors. After using this tool, the authors reviewed and edited the content as needed and take full responsibility for the content of the publication.

Acknowledgements

Korea Brain Research Institute Research Programs, grant 23-BR-01-01, 23-BR-03-01, 24-BR-03-08, and 23-BR-04-04 (JCR). National Research Foundation of Korea, funded by the Ministry of Science and Information and Communication Technology, grant NRF-2017M3A9G8084463 and NRF-2022R1A2C1004216 (JCR).

Author contributions

J.C.R. and J.H.C. planned the study. J.H.C. instrumented and performed the experiments. S.B. and J.P. analyzed the data under the supervision of J.C.R., J.H.C., J.W.C., and L.I.S. The manuscript was prepared by S.B. and J.C.R. with input from all the authors.

Competing interest

The authors declare no competing interests.

Supplementary information

Supplemental Figure S1: Time-correlation of activity dynamics along the coding direction by the PPC neurons in the STM task.

Supplemental Figure S2: Logic diagram of directional and non-directional phase-selective neurons identified by the modified General Linear Model (GLM).

Supplemental Figure S3: Reliability index of directional and non-directional neurons.

Supplemental Figure S4: Supplementary Figure 4. Phase selectivity of GLM-defined phase-selective and non-selective neurons.

Supplemental Figure S5: Anatomical distances and functional similarities.

Supplemental Figure S6: Reliability index of direction- and phase-selective neurons in error trials.

Supplemental Figure S7: Variance explained by the number of principal components.

Supplemental Figure S8: Discriminability between the trajectory distances and schematic of the trajectory similarity index (TSI)

Supplemental Figure S9: Framework of the proposed method for automatic event-related ROI detection.

Main Figure

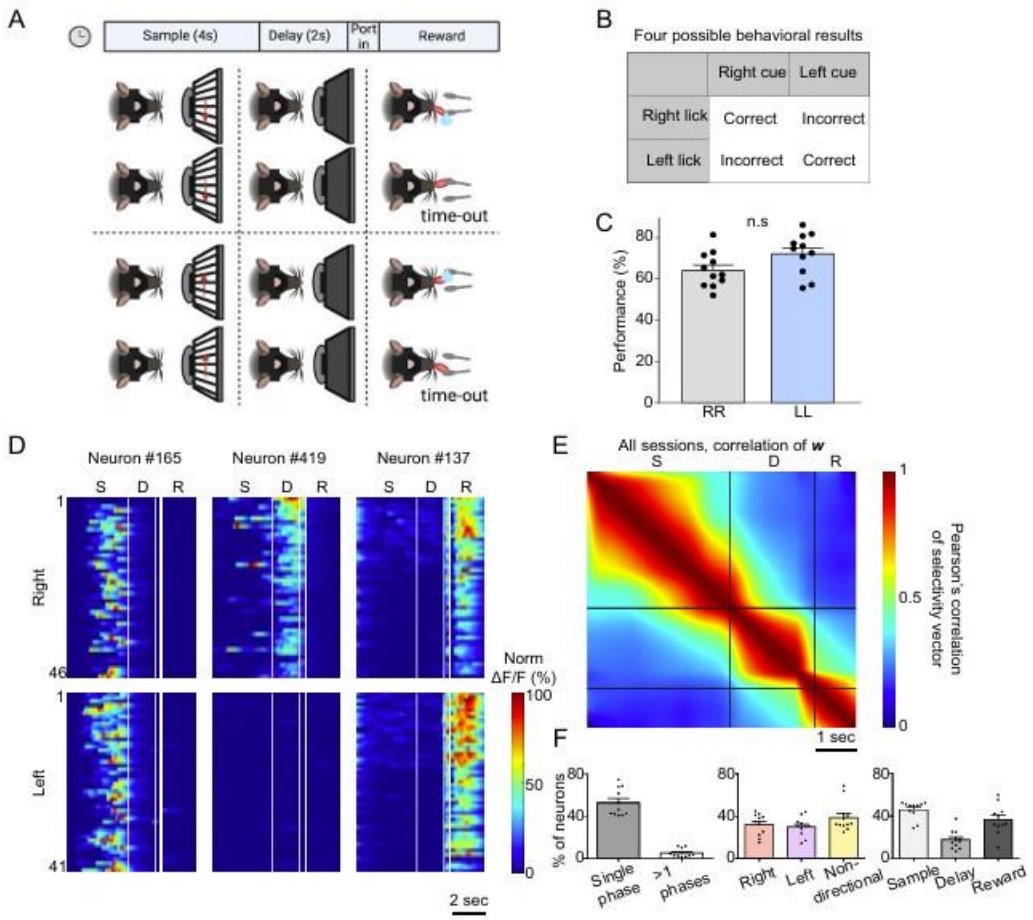

Figure 1 Ca^{2+} responses of PPC neurons during short-term memory task. A. The schematic illustrates the behavioral task designed to measure short-term memory in head-restrained mice. During the sample phase, black-and-white phase-reversing gratings moved either leftward or rightward (or downward or rightward) for 4 seconds on a screen in front of the mouse. After a 2-second delay, two laterally positioned lick ports were moved to a location within reach of the mouse's tongue. Correct licking of the corresponding lick port was rewarded with water, while incorrect licking resulted in a time-out as a form of punishment. **B.** Four possible behavioral outcomes from the task. **C.** Performance in right and left trials from thoroughly trained mice. No

significant difference was observed (two-tailed paired t-test; n=11, $p < 0.05$). Error bars represent the standard error of the mean (SEM) across sessions. n.s: not significant. **D.** Examples of neuronal activity recorded during behavioral tasks. Each row illustrates the color-coded normalized **Δ**F/F. **E.** The color-coded autocorrelation diagram of the mean response vectors, ***w***, derived from coding direction (CD) of correct trials. ***w*** was calculated over moving 0.5s time windows. Data from 11 sessions, 6 mice, and 4756 total neurons S: sample phase, D: delay phase, and R: response phase. **F.** The proportion of neurons displaying task-dependent activity defined by a General Linear Model (GLM). (Left) The fraction of neurons with single-phase selectivity, and neurons with activity in two or more phases out of all recorded neurons. (Middle) Percentages of neurons with and without directional selectivity out of single-phase selective neurons. (Right) Percentages of neurons with corresponding phase selectivity out of single-phase selective neurons.

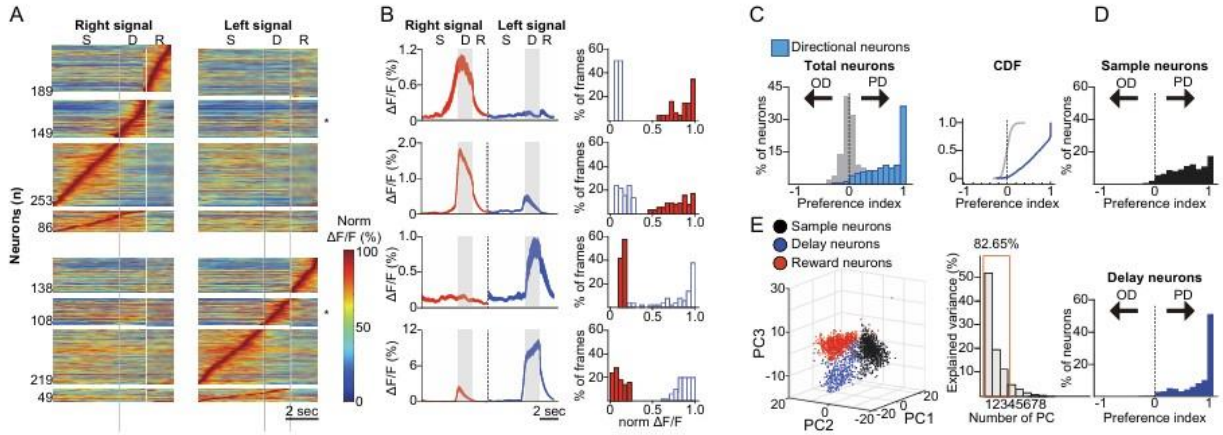

Figure 2 Identification and characterization of the direction- and phase-selective neurons. **A.** Color-coded trial average ΔF/F of right (upper) or left (lower) directional phase selective neurons. ΔF/F was normalized to the maximum ΔF/F and aligned based on the time-to-peak of each neuron. **B.** Example traces (left) and histogram of trial-averaged ΔF/F from highly directional phase-selective PPC neurons. The thickness of the traces represents the standard error. Blue and red in the histogram illustrate left and right trials, respectively. **C.** (Left) Histogram of preference indices (PI) of GLM-defined directional neurons (light blue) and those calculated with shuffled trials (gray). (Right) Same as left but shown as cumulative distribution function (CDF). **D.** PI histogram of directional neurons during the sample phase (upper) and delay phase (lower). **E.** Principal components analysis (PCA) capturing the temporal activity pattern of each neuron. GLM-defined sample (black), delay (blue), or reward (red) phase selectivity is indicated by colors. Variance explained by the principal components.

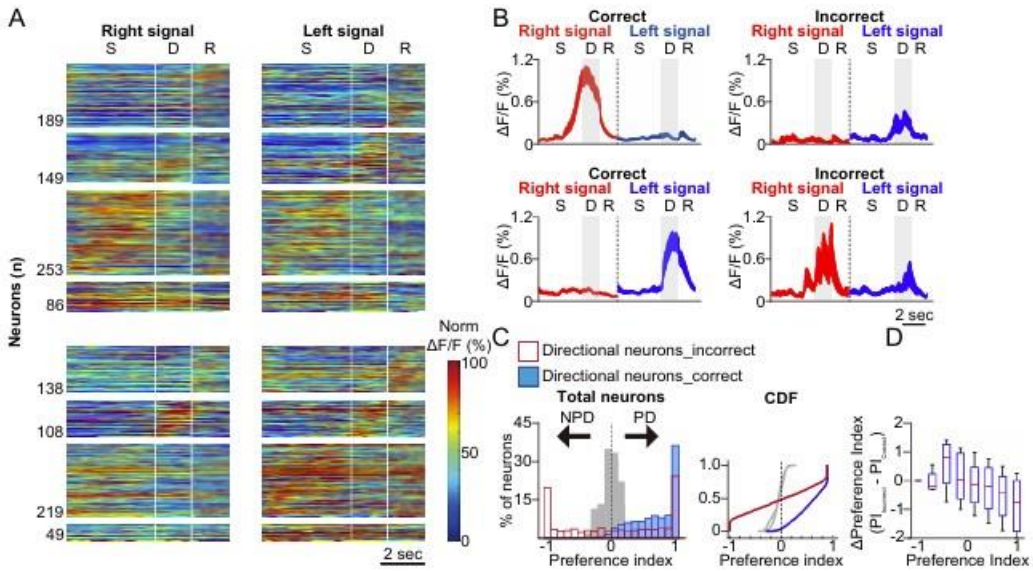

Figure 3. Responses of the direction- and phase-selective neurons in error trials. A. Same as Fig. 2A but in error trials. **B.** The same example neurons shown at the first and third row in Fig. 2B (left) and their mean traces in error trials. **C.** (Left) Histogram of preference indices (PI) of GLM-defined directional neurons in correct (light blue), error (red open), and shuffled (gray) trials. (Right) Cumulative distribution function (CDF) of the left histogram. **D.** A box plot illustrating the difference of PIs (ΔPI) between error and correct trials for each neuron, as a function of PIs in correct trials.

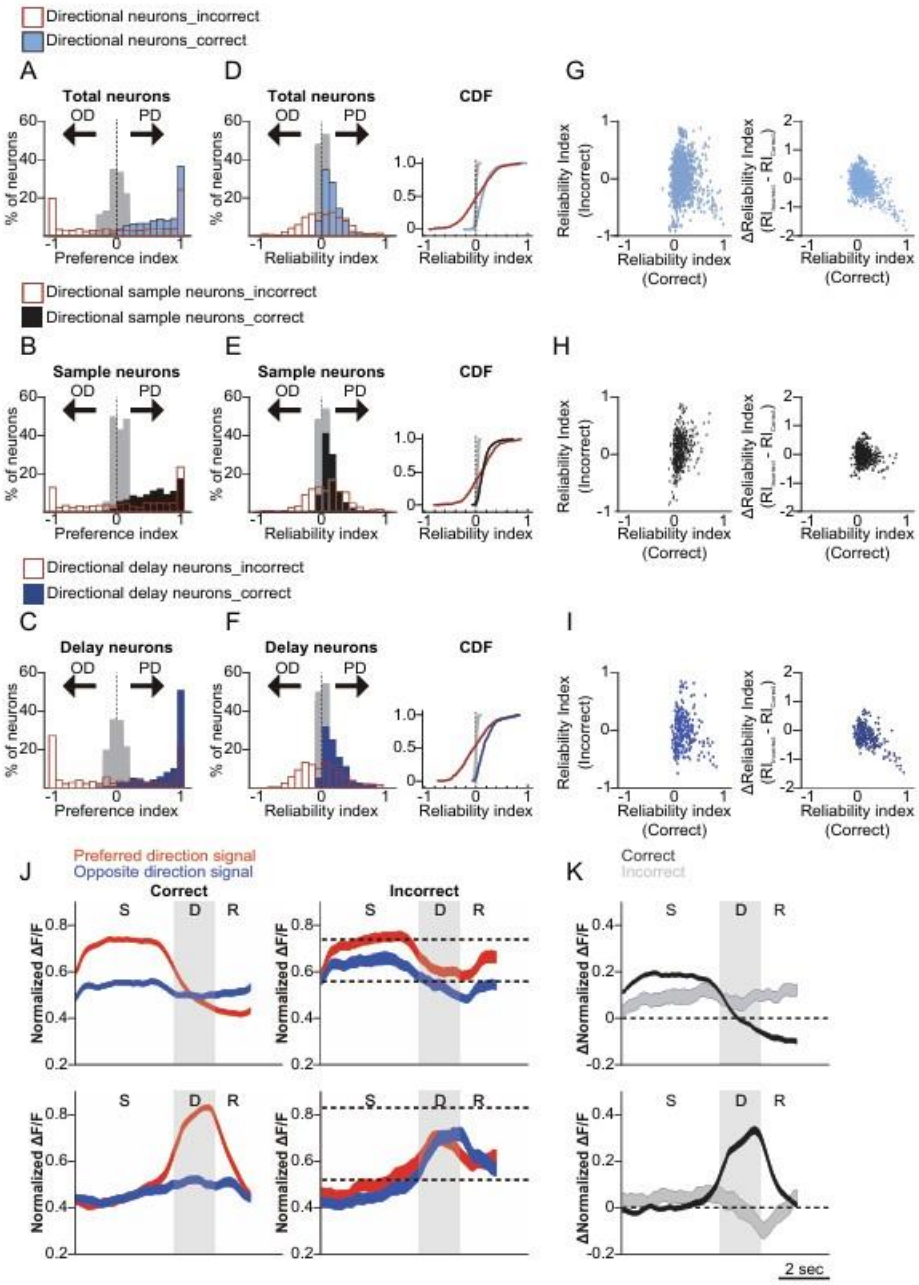

Figure 4. Comparison of responses between delay phase-selective neurons and sample phase-selective neurons during error trials. A. Preference indices (PI) histogram of GLM-defined directional single-phase selective neurons in correct (light blue), error (red open), and shuffled (gray) trials. **B.** PI histogram of directional sample-phase selective neurons in correct (black), error (red open), and shuffled (gray) trials. **C.** PI histogram of directional delay-phase

selective neurons in correct (blue), error (red open), and shuffled (gray) trials. **D.** (Left) Reliability indices (RI) histogram of GLM-defined directional single-phase selective neurons in correct (light blue), error (red open), and shuffled (gray) trials. (Right) Cumulative distribution function (CDF) of the left histogram. **E.** (Left) RI histogram of directional sample-phase selective neurons in correct (black), error (red open), and shuffled (gray) trials. (Right) Cumulative distribution function (CDF) of the left histogram. **F.** (Left) RI histogram of directional delay-phase selective neurons in correct (blue), error (red open), and shuffled (gray) trials. (Right) Cumulative distribution function (CDF) of the left histogram. **G.** (Left) Scatter plot comparing reliability index in PPC correct and incorrect. A reliability index value close to 1 for 'Correct' indicates a significant response in the preferred direction, while a reliability index value close to -1 for 'Incorrect' suggests a response closer to the opposite direction during error trials. (Right) Scatter plot comparing the reliability index (Correct) with the difference between reliability index (Incorrect) and reliability index (Correct) in PPC. Δ reliability index values closer to -1 indicate that the response during incorrect trials was closer to the opposite direction compared to correct trials. **H.** (Left) Scatter plot comparing the reliability index of GLM-defined direction-selective sample neurons in PPC during correct and incorrect trials. (Right) Scatter plot comparing the reliability index (Correct) of GLM-defined direction-selective sample neurons with the difference between the reliability indices for incorrect and correct trials. **I.** (Left) Scatter plot comparing the reliability index of GLM-defined direction-selective delay neurons in PPC during correct and incorrect trials. (Right) Scatter plot comparing the reliability index (Correct) of GLM-defined direction-selective delay neurons with the difference between the reliability indices for incorrect and correct trials. **J.** (Upper) Mean normalized ΔF/F of direction-selective sample neurons in response to the preferred (red) and the opposite (blue) directional signal in

correct (left) and incorrect (right) trials. (Lower) Same as upper plots but for direction-selective delay neurons. **K.** (Upper) Δ mean normalized ΔF/F of direction-selective sample neurons in correct trials (black) or incorrect trials (gray), calculated by subtracting the value of the opposite directional signal from the preferred directional signal. (Lower) (Upper) Δ mean normalized ΔF/F of direction-selective delay neurons in correct trials (black) or incorrect trials (gray), calculated by subtracting the value of the opposite directional signal from the preferred directional signal.

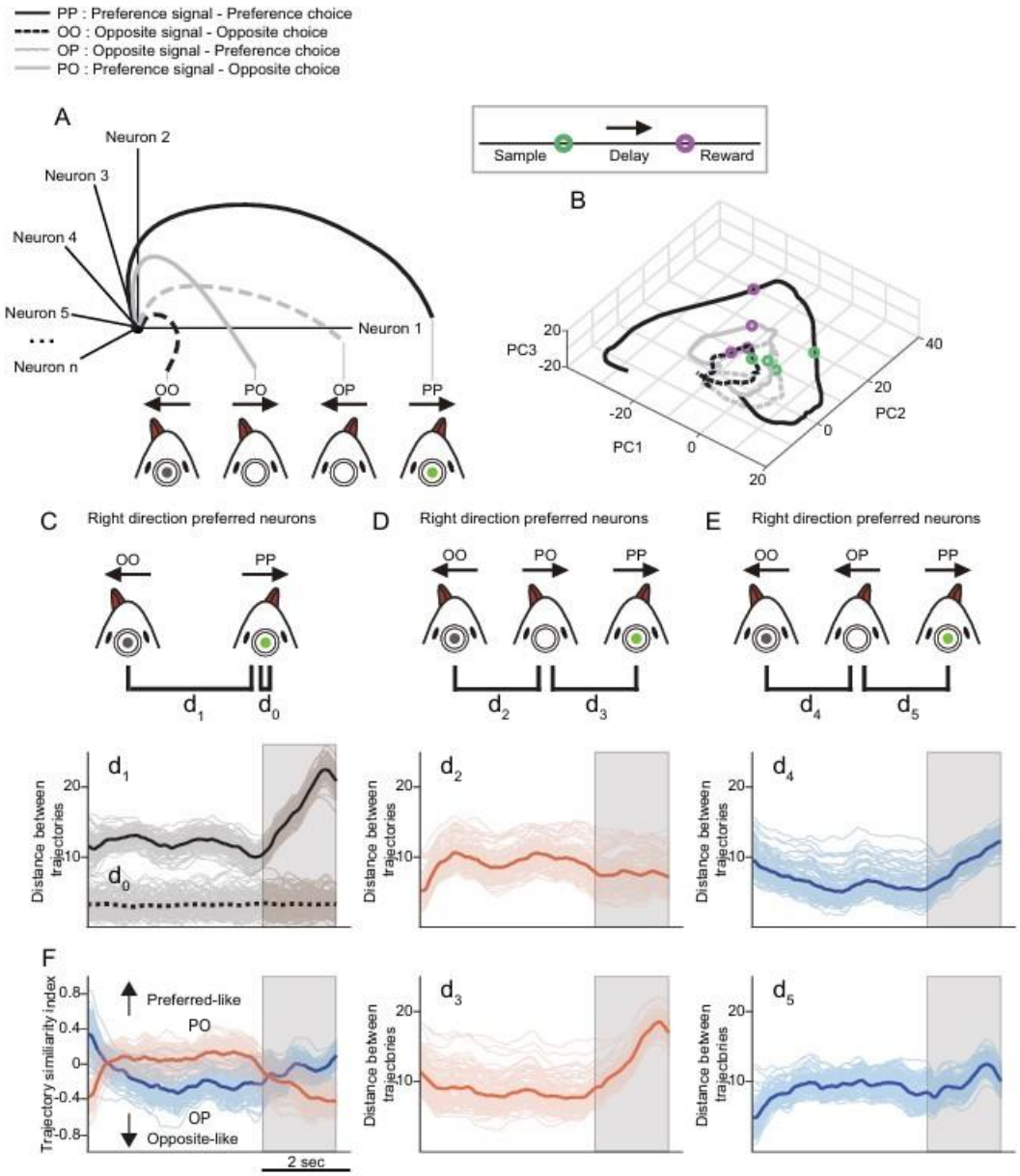

Figure 5. Differences in population activity of direction selective neurons in correct and error trials. A. Schematic of assessing population activity difference using the dimensionality reduction approach. **B.** Activity trajectories that capture the population activity of directional neurons in the preferred (dark colors) or opposite (light colors) directional stimulation in correct (blue) and incorrect (red) trials. Although the first three principal components are illustrated for

visualization purposes, trajectories were projected into a five-dimensional subspace. Eigenvector was generated using 50% of all sorted neurons, and the remaining 50% were projected onto this eigenvector. The faint lines in each graph represent values from 100 random iterations **C.** (Upper) A schematic of correct preferred and correct anti-preferred, or opposite trial (e.g. for left-preferring neurons, correct left trials vs. correct right trials). (Lower) Temporal changes of the Euclidean distance between the activity trajectories of correct preferred direction responses and correct opposite direction responses (PP-OO) (d1). d0 illustrates trial-by-trial activity variation, showing the distance between randomly selected preferred direction responses and the rest of the preferred direction responses in correct trials. **D.** d2: The distance between the activity trajectories of correct opposite direction responses and incorrect preferred direction responses. (PO-OO). d3: The inter-trajectory distance of correct preferred direction responses and incorrect preferred direction responses (PP-PO). **E.** d4: Inter-trajectory distance between the correct opposite direction response and incorrect opposite responses (OP-OO). d5: Inter-trajectory distance between the correct preferred direction response and incorrect opposite direction responses (PP-OP). **F.** Temporal changes in the trajectory similarity index for the incorrect preferred responses (orange) or the incorrect opposite responses (blue) (see also Supplementary Fig. 8).

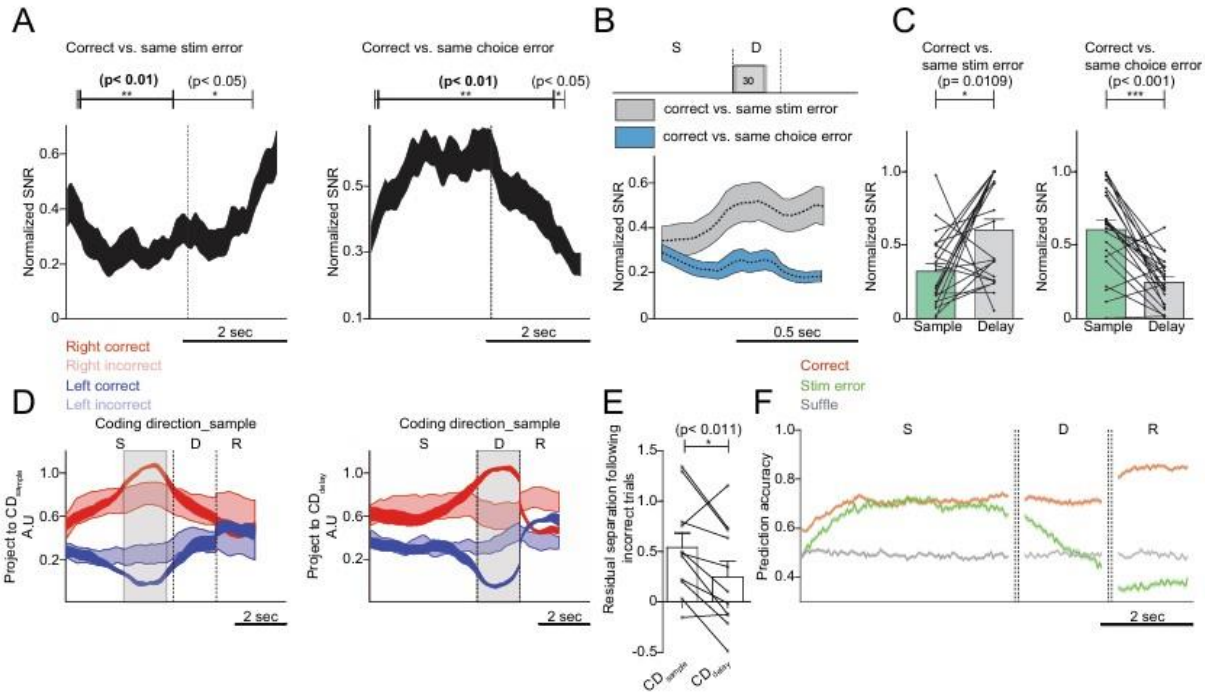

Figure 6. Population dynamics of PPC neurons in correct and incorrect trials. A. Time-dependent changes in the normalized signal-to-noise ratio (SNR) in distinction between responses in activity space using the linear discrimination task (LDA). SNR was calculated over a sliding window of 50 frames, advancing by one frame at a time. The vertical dashed line represents the initiation point where the window commences its entry into the delay phase. (Left) Mean normalized SNR between clusters of frames representing the ensemble of neural activity in correct trials and same stimulation error trials (i.e. LL vs LR and RR vs RL) as a function of time. The black horizontal line (paired t-test; frame 8 ~ 107, $p < 0.05$) and the bold black line (paired t-test; frame 11 ~ 65, $p < 0.01$) indicate time points significantly different from the delay phase. (Right) Same as left but between correct and same choice error trials (i.e. LL vs RL and RR vs LR). The black line (paired t-test; frame 3 ~ 112, $p < 0.05$) and the bold black line (paired t-test; frame 6 ~ 105, $p < 0.01$) indicate time points significantly different from the delay phase. Line thickness indicates mean ± SEM across sessions. **B.** Mean normalized SNR of LDA during

the delay phase. SNR was calculated over a sliding window of 30 frames during the delay phase. (Gray) LDA between correct trials and same stimulation error trials. (Blue) LDA between correct and same choice error trials as a function of time. The thickness of the lines represents standard error. **C.** Comparison of normalized SNR of LDA between correct and same stimulus error (left) or same choice error (right) calculated from the same number of frames in the sample phase (frames 66 ~ 115) and delay phase (frames 121 ~ 170). Statistical analyses were conducted using paired t-test (*$p < 0.05$, **$p < 0.01$, ***$p < 0.001$). Error bars indicate mean ± standard error across sessions. **D.** Projections of activity along CD_{sample} and CD_{delay} in each direction (red: right, blue: left) and response accuracy (dark: correct, light: incorrect). Line thickness indicates mean ± standard error across sessions. **E.** Residual separation defined as (Right incorrect - Left incorrect) / (Right correct - Left correct). (paired t-test, $p < 0.05$). **F.** Accuracy of decoded neural activity prediction by support vector machine (SVM) plotted as a function of time. Line thickness indicates mean ± standard error across sessions.

Methods

Animals

All animal experiments were conducted with the approval of the Animal Experiment Ethics Committee (approval no. IACUC-17-00031) at the Korea Brain Research Institute (KBRI). All experiments were performed using male C57BL/6J-Tg(Thy1-GCaMP6f)GP5.5Dkim/J transgenic Mice (n = 6).

Cranial window and head plate preparation

Mice aged between 8 to 12 weeks underwent cranial window and head plate implantation surgery. To ease pain and reduce inflammation, they received subcutaneous injections of ketoprofen (5 mg/kg) prior to surgery. For deep anesthesia, a mixture of 1–2% isoflurane or a ketamine/xylazine solution (100 mg/kg and 10 mg/kg) was used. After confirming anesthesia by the absence of pedal withdrawal reflex, we covered both eyes with petroleum jelly and removed hair from the incision site. The scalp was cleaned and sterilized with ethanol and betadine and then removed. Using a scalpel, we stripped away the periosteum and roughened the skull's surface with a drill burr (Miniature Carbide Burr Drill Bits Set, Stoelting) to ensure the dental cement would adhere properly. The skull was cleaned with Ringer solution, and a craniotomy approximately 3 mm in diameter was performed over the posterior parietal cortex of the right hemisphere. The craniotomy was then sealed with a double-layered glass coverslip (round 3/5 mm, Harvard Apparatus combined with NOA71, Norland) and secured with surgical adhesive (Vetbond, 3M). The dura mater remained unharmed. A tailor-made commercially pure titanium head plate (rectangular shape, 19 mm x 12 mm x 1 mm) with a 4.5 mm central opening was

affixed on top of the window using dental cement (Super-Bond C&B kits, Sun Medical, darkened with black pigment). After the surgery, mice were placed in a warmed chamber for a minimum of four hours for recovery and post-operative monitoring. Consequently, the animals were housed in individual cages.

Behavior task

After full recovery from surgery, the mice were provided with limited water (1 ml/day) while their body weights were monitored. If a mouse's body weight dropped below 75% of its initial weight, water restriction and training were stopped. The mice were trained to perform a delayed match-to-sample task while their heads were fixed in place using a holder (modified MAG-1, Narishige Scientific Instrument, Tokyo, Japan). The visual signal to discriminate was high-contrast sine-squared wave gratings, moving either left/right or down/right, with specific spatial (3 cm/cycle) and temporal (2 Hz) frequencies. The signal was provided by a monitor placed directly in front of the mice at a distance of 25cm. Custom written software running in Raspberry Pi 3 (RPi3) was used for both stimuli generation and behavioral training. Left/right or down/right were trained in a separate group of mice and all the behavioral and imaging data acquired from left and down trials were pooled and analyzed as the same group.

The position of the drinking spouts was adjusted to fit each individual mouse. The lick detection circuit and reward solenoid were controlled by Arduino Mega2560 (rev 3, Arduino) connected to RPi3. During training, mice earned the majority of their daily water intake (1 mL) through training. Each visual stimulus lasted 4 seconds, followed by a 2-second pause. After this pause, the spouts moved quickly to a position accessible by the tongue for 1 second. Successful licks (licks on the left-hand side spout in response to leftward or downward moving signals, or licks

on the right-hand side spout in response to rightward moving signals) during this window were rewarded with approximately 5 µl of tap water. Incorrect licks resulted in no reward and were punished with a 2-second time-out, after which the trial continued. After a reward period or upon an incorrect lick, the spout withdrew quickly, staying out of reach until the commencement of the next trial, which was set to begin 4 or more seconds later. Training progressed through the following stages. First, the mice learned to lick a non-moving lick port located at the center with either of visual cues. Then they learned to match the direction and rewarding spout out of the two non-moving spouts. We then gradually increased the delay by introducing moving lick ports. Once mice consistently achieved high performance (>70% correct rate) with 2s delay, behavioral performance and PPC activities were recorded for analyses.

In vivo two-photon calcium imaging

We conducted two-photon imaging utilizing HyperScope (Scientifica) and ScanImage (MBF Bioscience) with a Ti:Sapphire laser (Chameleon Ultra II, Coherent). The imaging setup targeted the GCaMP6f calcium indicator excited at 910 nm through an 16x water immersion lens (N16XLWD-PF, Nikon). The objective lens has an attached light barrier (custom made) isolating the imaging system from visual stimuli. We captured 512 × 512 pixel images(700umX700um ROI) at 30Hz in the PPC layer 2/3. The average imaging laser power was less than 100mW at the objective lens. The imaging and behavior system was synchronized by frame trigger signal output counted by Mega 2560.

Image preprocessing and cell selection

The processing of calcium imaging data utilized the CaImAn software framework. This included adjusting for motion in segments of 128 by 128 pixels, ensuring each segment overlapped by 48 pixels to maintain continuity. For identifying neuronal sources, we applied the 'greedy_roi' technique, sizing the expected neurons at 4 by 4 pixels for detailed imaging and 3 by 3 pixels for imaging the entire brain. Only components with a signal-to-noise ratio of at least 2.0 and 90% pixel correlation were considered reliable. We normalized the fluorescence signal decay rates, 3.0 seconds for indicators localized in the nucleus and 1.0 second for those in the cytosol, using z-scoring for subsequent analyses. To ensure coherence between behavioral actions and neural activity, we aligned and adjusted all time series data to a uniform sampling rate of 30 Hz, synchronized with the camera and microscope's frame capture times

Automated event-related neuron detection in calcium imaging data

We used generalized linear models (GLM) to regress recorded calcium signals against a time series of task events. We propose a novel method for automatically searching event-related neurons in calcium imaging data (Supplementary Fig. 9). Our method searches the ROI pixelwise using event timing information. By utilizing a statistical method to determine the relationship between the calcium trace of each pixel and the event timing, the searched ROI pixels are clustered. This process enables the automatic detection of event-related ROIs without requiring any additional detection procedures, while also enabling the detection of components with low SNR or fine size as ROI.

The proposed method determines the event relevance of calcium traces to detect event-related neurons in calcium imaging data. Rather than relying on the morphological shape of the neuron for ROI detection, the proposed method determines the event relevance of each pixel's calcium

trace independently. If ROI detection is performed by reflecting the neuron's morphological shape, the detection performance may decrease with low SNR or fine-size components.

The proposed method utilizes a generalized linear model (GLM) to detect ROIs by assessing the relationship between the calcium trace of each pixel and the calcium signal model that is strongly associated with the event. To create a calcium signal model that is strongly associated with events, a temporal component model of calcium dynamics and event timing is necessary.

Event timing refers to the timing of a task or stimulus. In an event-related neuron, there is a calcium activity after at the event timing. Non-event timing refers to other times where there are just activations that are not related to events, including spontaneous activation occurs. Neurons strongly associated with events show high activation at event timing while low activation at non-event timing. Therefore, we define a spike train $\tilde{s}(t)$ of the calcium signal most strongly associated with the event:

$$\boldsymbol{\tilde{s}(t) = \sum_{i=1}^{k} \beta_i \delta(t - t_i)} \tag{1}$$

where $\tilde{s}(t)$ is composed of the product of the β (amplitude of the spike) and the impulse train. An event-related neuron is expected to activate at least once after an event. Denoting the ith event timing by t_i, $\tilde{s}(t)$ becomes a spike train of event-related neurons with an amplitude of $\beta_i$at event timings.

The temporal component of calcium dynamics is determined by the activity of a calcium indicator. When the calcium indicator is combined with calcium, luminous intensity changes. The fluorescence trace of the calcium indicator was modeled in the form of a double exponential and is expressed as:

$$\boldsymbol{c(t) = e^{\frac{-t}{\tau_d}} - e^{\frac{-t}{\tau_r}}} \tag{2}$$

where τ_r and τ_d are the time constants for the increase and decrease of fluorescence, respectively[1].

We express the modeled event-related calcium trace $\tilde{y}(t)$ of the neuron by the fluorescence trace model of the calcium indicator $c(t)$ with the convolution of the spike train $\tilde{s}(t)$.

$$\boldsymbol{\tilde{y}(t) = \int_{-\infty}^{\infty} \tilde{s}(t-\tau)c(\tau)\, d\tau} \tag{3}$$

We defined the event-related calcium trace model $\tilde{y}(t)$. The ROI was detected by determining the relationship between this model and the pixel's calcium trace $y(t)$ using the least square method and 1-sampled *t*-test. Through the least square method, it is possible to find the estimator of the regression coefficient β (the amplitude of the spike in equation (1)) that minimizes the residual of the pixel's calcium trace $y(t)$ and the event-related calcium trace model $\tilde{y}(t)$ of the neuron. The β estimator matrix $\hat{\beta}$ up to the kth event was expressed as:

$$\boldsymbol{\hat{\beta} = [\beta_1\ \ \beta_2\ \ \beta_3\ \ \cdots\ \ \beta_k] = \|y(t) - \tilde{y}(t)\|^2} \tag{4}$$

Notice that $\tilde{y}(t)$ has a weight $c(t)$ for event timing. By $c(t)$, as the event timing and activation timing are closer, the value of the regression coefficient β increases. It was determined whether a neuron is event-related through the distribution of β. As the mean of $\hat{\beta}$ is close to 0 or the variance of $\hat{\beta}$ is larger, the activation timing of neurons has little relation to the event timing.

Therefore, we tested the null hypothesis that β is extracted from a normal distribution with a zero mean and unknown variance, using a 1-sampled *t*-test. At this time, the test statistic is as shown:

$$test\ statistic = \frac{\bar{\beta}}{s/\sqrt{k}} \tag{5}$$

where $\underline{\beta}$ is the mean of the $\hat{\beta}$, s is the standard deviation of the $\hat{\beta}$, and k is the size of $\hat{\beta}$, also known as the trial number of events. The proposed method uses a p-value of 0.05 to determine a pixel with a statistically significant difference from a pixel of an event-related neuron.

When the event association determination is completed for all pixels of the calcium image, the proposed method finally defines the event-related ROI by clustering the pixels associated with the event. The proposed method clusters pixels to ROIs automatically, where the clustering is performed based on the Moore-Neighbor tracking algorithm and determines connectivity between pixels [2]. Finally, the proposed method provides ROI clusters corresponding to event-related neurons (Supplementary Fig. 9).

Selectivity

Through our uniquely developed Generalized Linear Model (GLM), we pinpointed neurons that were activated in specific phases across different behavioral patterns. To confirm these observations, we employed a preference index, calculated by conducting a receiver operating characteristic (ROC) analysis. This analysis measures the theoretical observer's capability to distinguish between types of trials using the neural responses from individual trials. The preference index itself is determined from the area under the ROC curve (auROC), using the

formula $2 \times (auROC - 0.5)$, producing a range from -1 to 1. We applied this index to the segments representing each behavioral phase, using the average neural activity from trials to derive specific values. Notably, the preference index (PI) compares trial-averaged values between right and left conditions. Additionally, the reliability index (RI) is calculated by comparing all individual trials between right and left, without averaging. Furthermore, the phase selective index (PSI) is derived by comparing the trial-averaged values from the phase of interest with those from non-related phases. This method allowed us to quantitatively assess the degree to which individual neurons preferentially respond to different trial types, providing a clearer understanding of the role each sorted neuron plays in the observed behavioral patterns.

PCA

We used Principal component analysis (PCA) on the neurons sorted through the Generalized Linear Model (GLM) to infer a shared space, an intrinsic manifold shared by neuronal population activity. We calculated the variance explained by principal components of correct trials. We observed five principal components explained similar level of variance of our data both in right-preferring neurons, left preferring neurons, and directional neurons.(right-preferring neurons: 72.4%, left-preferring neurons: 69.0%, directional neuron: 70.4%). A specific procedure for conducting PCA on PPC neuron data is as follows:

We organized the optical data from an experiment into an $X = M \times N$ matrix, where M is the number of frames per trial, and N is the number of sorted neurons in a session $\left(N = N_{sample} + N_{delay} + N_{reward}\right)$. Directional neurons, comprising both right-preferring and left-preferring neurons, were grouped together. Therefore, we proceeded with Principal Component Analysis (PCA) after aligning each neuron according to its preferred direction. We applied z-score

normalization to each column of the matrix to ensure comparability across neurons. Z-score normalization adjusts the data to have a mean of 0 and a standard deviation of 1, enhancing the robustness of PCA against variations in scale among different neurons.

$$\boldsymbol{Z_{correct}} = \frac{(\boldsymbol{X} - \boldsymbol{\mu})}{\boldsymbol{\sigma}} \tag{6}$$

Where μ is the mean and σ is the standard deviation of neuron activity.

We calculated the covariance matrix, C, from the normalization data Z, to understand how the variables relate to one another.

$$\boldsymbol{C_{correct}} = \frac{\boldsymbol{1}}{\boldsymbol{n-1}} \boldsymbol{Z_{correct}^{T} Z_{correct}} \tag{7}$$

Where n is the number of neurons.

We computed the eigenvalues and eigenvectors of the covariance matrix C. The eigenvectors represent the directions of maximum variance in the data, and the eigenvalues represent the magnitude of these variances. Neuronal activity data were projected onto the principal components to transform the data into a new space defined by these components. To compute relative changes in incorrect trials compared to correct trials, we projected the incorrect trials onto the eigenvector induced by correct trials and quantified the variations through the distances between trajectories.

$$\boldsymbol{Z_{pca}} = \boldsymbol{Z_{incorrect}} \times \boldsymbol{V_{correct}} \tag{8}$$

Where $V_{correct}$ represents eigenvectors and Z_{pca} represents the data transformed into the principal component space.

Coding direction

This procedure closely follows the methodology outlined in [3,4]**.** The population dynamics of n neurons captured concurrently throughout a session were examined (Fig. 6). The population activity of n neurons created a trajectory in the n - dimensional activity space during each session, where each dimension corresponds to a single neuron activity. In the activity space, we found directions (modes) that maximally separated the neuronal pathways for various trial conditions and specific phase. In trials with lick-correct left and lick-correct right instructions, the trial-averaged activity differences of n neurons were averaged within a 1.7s (121 ~ 170 frame) window after the visual cue offset. This resulted in the delay mode (CD_{delay}), which was calculated as follows:

$$\Delta \underline{\boldsymbol{r}} = \underline{\boldsymbol{r}}_{\boldsymbol{correct\ right}} - \underline{\boldsymbol{r}}_{\boldsymbol{correct\ left}} \tag{9}$$

The resulting vector was normalized by its l^2 norm, resulting in a vector of weights (one weight per neuron i) as follows:

$$m = \frac{\Delta \bar{r}}{\sqrt{\sum_i^N |\Delta \bar{r}_i|^2}} \tag{10}$$

Projections of the neural activity along the mode over time were calculated as follows:

$$\boldsymbol{P^k} = (\boldsymbol{X^k})^{\boldsymbol{T}}\boldsymbol{m} \tag{11}$$

Where X^k is the $N \times T$ matrix of averaged activity of neurons over time for session k.

To maintain consistency in the analysis despite the varying number of neurons recorded in each trial, we normalized each mode by its l^2 norm, as indicated in equation (10). This normalization ensured that the projected neural activity, P^k remained unaffected by the quantity of neurons simultaneously recorded. In instances where a specific neuron was not showed a specific activity during a particular trial, we assigned a weight of zero to that neuron in both equations (10) and (11) for the purpose of calculating the projected activity for that trial. This approach guaranteed that the analysis could accurately reflect the contribution of active neurons in each trial, without skewing results due to differences in neuron sampling across trials.

The sample mode (CD_{sample}) and the reward mode (CD_{reward}) were defined to capture distinct aspects of neural activity corresponding to different phases of the trials, specifically focusing on the behavioral outcomes of licking correctly to the right or left.

CD_{sample} : This mode was determined by constructing an $n \times 1$ vector representing the differences in the average activity of n neurons during trials that resulted in correct licks to the right or left. These differences were averaged over a 1.7-second window (from frame 56 to frame 115) coinciding with the beginning of the stimulus presentation. By focusing on this early window, CD_{sample} captures the neural activity patterns triggered by the initial stimulus, reflecting how neurons differentiate between trial types in response to the stimulus.

CD_{reward} : Similarly, this mode was defined by an $n \times 1$ vector, but it focused on the average activity differences of n neurons during trials with correct licks to the right or left, within a 1-second window (from frame 171 to frame 200) at the conclusion of the delay phase. The CD_{reward} specifically targets the neural response patterns associated with the anticipation or receipt of a reward, highlighting how neuronal activity aligns with behavioral outcomes following the stimulus-response interval.

In addition to the selective modes that focused on differentiating neural activity based on specific trial outcomes, we identified a nonselective ramping mode (D_{reward}). This mode was designed to capture general changes in neural activity towards the end of the delay phase, irrespective of the trial outcome (whether the lick was correct to the right or left). To compute this ramping mode, we adopted a methodology similar to that used for the reward mode. However, instead of distinguishing between trial outcomes, we aggregated neural responses from both correct-right and correct-left licks. We then calculated the difference in trial-averaged activity during the last second of the delay phase (from frame 141 to frame 170) compared to the first second of the reward phase (from frame 171 to frame 200).

$$\Delta \underline{\boldsymbol{r}} = \underline{\boldsymbol{r}}_{\boldsymbol{correct\ reward}} - \underline{\boldsymbol{r}}_{\boldsymbol{correct\ last\ delay}} \tag{12}$$

To facilitate a direct comparison between the sample and delay phases while considering their distinct neural dynamics, we employed the Gram-Schmidt process for orthogonalization of these phases in a specific sequence. This process was applied to the modes in two different orders: first, starting with the CD_{reward}, then the D_{reward}, followed by the CD_{sample}; and second, beginning with the CD_{reward}, then the D_{reward}, and finally, the CD_{delay}. Orthogonalization

using the Gram-Schmidt process ensures that each mode represents a unique aspect of neural activity, independent of the others, thus allowing for a clearer analysis of the distinct contributions of sample and delay phases to overall neural dynamics.

Furthermore, to assess the neural activity's alignment with behavioral outcomes - specifically, the differences between correct and incorrect responses - we projected the trial-averaged activity from incorrect trials onto the modes defined by correct trials across sessions. This projection allowed us to compare the neural activity associated with correct and incorrect trials within the same mode, providing insights into how specific patterns of neural dynamics correlate with behavioral performance. This approach helps in understanding the neural underpinnings of decision-making and error processing by quantifying the extent to which neural activity during incorrect trials deviates from the established patterns of correct trials.

After projecting the neural activity data along the direction defined by CD (which represents the difference in neural activity between conditions), we normalized the resulting projections. This normalization involved adjusting the projections based on the average value obtained from correct rightward trials during the specific phase associated with each mode, for every session. This step ensures that the comparison across different trials and sessions is on a consistent scale, facilitating a more accurate analysis of the neural activity patterns.

To further investigate the differences in neural activity patterns between incorrect and correct trials, we introduced the concept of "residual separation." This metric quantifies the deviation in the neural trajectories of incorrect trials from those of correct trials. The residual separation effectively captures the extent to which the neural representation of incorrect trials diverges from the expected pattern observed in correct trials, providing insights into the neural mechanisms underlying error processing and decision-making accuracy. This analysis allows us to better

understand how the brain's neural activity aligns with behavioral outcomes and how it adapts or fails in cases of incorrect responses.

$$\boldsymbol{Residual\ separation} = \frac{\boldsymbol{mean(Traj_{incorrect\ right})} - \boldsymbol{mean(Traj_{incorrect\ left})}}{\boldsymbol{mean(Traj_{correct\ right})} - \boldsymbol{mean(Traj_{correct\ left})}} \tag{13}$$

Mean ($Traj$) represents averaged trajectory at the time corresponding to each mode.

Linear discriminant analysis

This procedure closely follows the methodology outlined in[5]

In examining a neural network that processes stimulus-tuned input under noisy conditions, with the objective of accurately reporting the stimulus identity, we delve into the nature of the input signals. Assuming that for a particular stimulus, the input time series can be modeled by a multivariate normal distribution characterized by temporally uncorrelated, stimulus-independent noise, our analysis reveals a statistically optimal strategy for distinguishing between two different stimuli. This strategy encompasses executing a linear projection alongside temporal filtering of the input time series.

By applying this approach, we calculate the ideal projection weights and filtering mechanism, alongside the signal-to-noise ratio (SNR) achievable through any given projection and filtering combination. It's important to highlight that the selection of the input dimensionality and statistical properties was guided primarily by the aims of enhancing visualization and deepening conceptual understanding. However, our analytical framework is versatile, accommodating inputs from an arbitrary number of neurons, each with unique stimulus tuning and noise

covariance patterns. This flexibility underscores the broad applicability of our findings, extending beyond specific configurations to encompass a wide range of neural input scenarios. For the task of distinguishing between two types of stimulations S_i , where $i = 1$ corresponds to a correct right decision and $i = 2$ to a correct left decision, we consider the dynamics of feedforward input at each time step t. The input, $u(s_i, t)$, follows a multivariate normal distribution, characterized by a stimulus-dependent mean and a stimulus-independent covariance. Specifically, the mean for the stimulation S_1 is denoted as $g(s_1) = [1, 2]$, and for S_2 it is $g(s_2) = [2, 1]$. The covariance matrix, independent of the stimulus, is given by $\sum_\eta = [2, 1; 1, 2]$. To analyze the inputs, we employ a projection onto a linear discriminant defined by $\mathrm{W}_{LD} = \sum_\eta^{-1}(\mathrm{g}(\mathrm{s}_2) - \mathrm{g}(\mathrm{s}_1))$.This approach effectively differentiates the inputs based on their stimulus-dependent means while considering the uniform noise structure. The projected time series, $d_{W_{LD}}(s, t) = w_{LD}^T u(s, t)$ then undergoes cumulative summation over time to yield $D_{W_{LD}}(s, t) = \sum_{t'=1}^{t} \mathrm{d}_{\mathrm{W}_{LD}}(s, t)$.

This methodology leverages the linear discriminant W_{LD} to filter and aggregate the signal in a way that enhances the separation between the two stimuli. By summing the projected signals cumulatively, the process amplifies the distinction between the neural responses to S_1 and S_2, facilitating the identification of the stimulus based on the accumulated evidence over time.

To elucidate the processing of instantaneous input $u(s, t)$ onto a vector w, we derive expressions for the signal difference ($\Delta\mu_{input}(w)$), noise ($\sigma_{input}(w)$), and signal-to-noise ratio (SNR) associated with the projection $d_w(s, t) = w^T u(s, t)$. The analytical expressions are as follows:

$$\Delta\boldsymbol{\mu}_{\boldsymbol{input}}(\boldsymbol{w}) \equiv \langle \boldsymbol{d}_{\boldsymbol{w}}(\boldsymbol{s}_2, \boldsymbol{t}) - \boldsymbol{d}_{\boldsymbol{w}}(\boldsymbol{s}_1, \boldsymbol{t}) \rangle = \boldsymbol{w}^{\boldsymbol{T}}\big(\boldsymbol{g}(\boldsymbol{s}_2) - \boldsymbol{g}(\boldsymbol{s}_1)\big) \tag{14}$$

Signal difference ($\Delta\mu_{input}(w)$) is the difference in mean projections between the two stimuli. It quantifies how distinct the mean responses to the two stimuli are when projected onto $\boldsymbol{w}$.

$$\sigma_{input}(\mathrm{w}) \equiv \sqrt{0.5\sum_{i=1,2}\langle(d_w(s_i,t) - \langle d_w(s_i,t)\rangle)^2\rangle} = \sqrt{\mathrm{w}^T\sum_{\eta}\mathrm{w}} \tag{15}$$

Noise ($\sigma_{input}(w)$) is the standard deviation of the projection. It measures the variability of the projection, irrespective of the stimulus.

$$\boldsymbol{SNR_{input}(w) = \Delta\mu_{input}(w)/\sigma_{input}(w)} \tag{16}$$

Signal to noise ratio (SNR) assesses the clarity of the signal relative to the noise for the chosen projection vector $\boldsymbol{w}$.

Following temporal integration, to calculate the cumulative effect over time, we consider $D_w(s,t) = \sum_{t'=1}^{t} d_w(s,t')$ and derive the temporally integrated quantities:

$$\boldsymbol{\Delta\mu_{input}(w,t) \equiv \langle D_w(s_2,t) - D_w(s_1,t)\rangle = \Delta\mu_{input}(w)t} \tag{17}$$

Integrated signal difference ($\Delta\mu_{input}(w,t)$) grows linearly with time, reflecting how the separation between stimuli accumulates over time.

$$\sigma_{input}(\mathrm{w}, t) \equiv \sqrt{0.5 \sum_{i=1,2} \langle (D_w(s_i, t) - \langle D_w(s_i, t) \rangle)^2 \rangle} = \sigma_{input}(\mathrm{w})\sqrt{t} \tag{18}$$

The standard deviation of the integrated signal scales with the square root of time. Integrated noise ($\sigma_{input}(w, t)$) indicates how noise accumulates over time.

$$\boldsymbol{SNR_{input}(w, t) \equiv \Delta\mu_{input}(w, t)/\sigma_{input}(w, t) = SNR_{input}(w, t)\sqrt{t}} \tag{19}$$

Integrated SNR ($SNR_{input}(w, t)$) demonstrates how the clarity of the signal improves with temporal integration, as the signal difference accumulates faster than noise over time.

The trials were organized into four categories based on the mouse's response to directional cues, enabling a precise analysis of behavioral patterns:

(1) Trials where the mouse licked right in response to a right-directed cue. (2) Trials where the mouse licked left in response to a left-directed cue. (3) Trials where the mouse licked left in response to a right-directed cue. (4) Trials where the mouse licked right in response to a left-directed cue.

The linear discriminant (w_{LD}) was determined based on the differentiation between the two types of stimulus inputs in correctly responded trials.

To assess the SNR within the time-series data meticulously, we employed a specific windowing technique. A window spanning 50 frames was defined, and this window was progressively shifted by one frame forward to scrutinize the SNR variations across the different groups over time. The SNR within each window was computed as the ratio of the mean signal activity to the

mean noise activity, enabling a quantitative measurement of how clearly the signal of each group stood out against the background noise.

To standardize comparisons across different sessions and ensure a uniform basis for analysis, the SNR values observed were normalized against the maximum SNR value observed in the respective session. This step was critical for drawing direct comparisons across sessions, effectively illuminating the signal quality differences between them. The utilization of Matlab for all data analyses provided a robust framework for dissecting and understanding the dynamic processes underlying the behavioral responses.

Data availability

The data and custom MATLAB analysis code supporting the findings of this study are available on Figshare at 10.6084/m9.figshare.26778301

Reference

1. Lee, J., and Park, S. (2005). Working memory impairments in schizophrenia: A meta-analysis. J Abnorm Psychol *114*, 599–611.

2. Reichenberg, A., Caspi, A., Harrington, H., Houts, R., Keefe, R.S.E., Murray, R.M., Poulton, R., and Moffitt, T.E. (2010). Static and dynamic cognitive deficits in childhood preceding adult schizophrenia: A 30-year study. American Journal of Psychiatry *167*, 160–169.

3. Forbes, N.F., Carrick, L.A., McIntosh, A.M., and Lawrie, S.M. (2009). Working memory in schizophrenia: a meta-analysis. Psychol Med *39*, 889–905.

4. Chafee, M. V, and Goldman-Rakic, P.S. (1998). Matching Patterns of Activity in Primate Prefrontal Area 8a and Parietal Area 7ip Neurons During a Spatial Working Memory Task. J Neurophysiol *79*, 2919–2940.

5. Chafee, M. V, and Goldman-Rakic, P.S. (2000). Inactivation of Parietal and Prefrontal Cortex Reveals Interdependence of Neural Activity During Memory-Guided Saccades. J Neurophysiol *83*, 1550–1566.

6. Harvey, C.D., Coen, P., and Tank, D.W. (2012). Choice-specific sequences in parietal cortex during a virtual-navigation decision task. Nature *484*, 62–68.

7. Zingg, B., Hintiryan, H., Gou, L., Song, M.Y., Bay, M., Bienkowski, M.S., Foster, N.N., Yamashita, S., Bowman, I., Toga, A.W., et al. (2014). Neural networks of the mouse neocortex. Cell *156*, 1096–1111.

8. Shadlen, M.N., and Newsome, W.T. (2001). Neural basis of a perceptual decision in the parietal cortex (area LIP) of the rhesus monkey. J Neurophysiol *86*, 1916–1936.

9. Hanks, T.D., Kopec, C.D., Brunton, B.W., Duan, C.A., Erlich, J.C., and Brody, C.D. (2015). Distinct relationships of parietal and prefrontal cortices to evidence accumulation. Nature *520*, 220–223.

10. Save, E., and Poucet, B. (2009). Role of the parietal cortex in long-term representation of spatial information in the rat. Neurobiol Learn Mem *91*, 172–178.

11. Nitz, D.A. (2006). Tracking Route Progression in the Posterior Parietal Cortex. Neuron *49*, 747–756.

12. Mcnaughton, B.L., Mizumori, S.J.Y., Barnes, C.A., Leonard, B.J., Marquis, M., and Green, E.J. (1994). Cortical Representation of Motion during Unrestrained Spatial Navigation in the Rat. Cerebral Cortex *4*, 27–39.

13. Krumin, M., Lee, J.J., Harris, K.D., and Carandini, M. (2018). Decision and navigation in mouse parietal cortex. Elife *7*.

14. Goard, M.J., Pho, G.N., Woodson, J., and Sur, M. (2016). Distinct roles of visual, parietal, and frontal motor cortices in memory-guided sensorimotor decisions. Elife *5*.

15. Shenoy, P., and Yu, A.J. (2012). Strategic Impatience in Go/NoGo versus Forced-Choice Decision-Making. NeurIPS.

16. Oh, S.W., Son, S.J., Morris, J.A., Choi, J.H., Lee, C., and Rah, J.C. (2021). Comprehensive Analysis of Long-Range Connectivity from and to the Posterior Parietal Cortex of the Mouse. Cereb Cortex *31*, 356–378.

17. Kleinfeld, D., Giovannucci, A., Friedrich, J., Gunn, P., ré mie Kalfon, J., Brown, B.L., Ann Koay, S., Taxidis, J., Najafi, F., Gauthier, J.L., et al. (2019). CaImAn an open source tool for scalable calcium imaging data analysis. Elife.

18. Nelder, J.A., and Wedderburn, R.W.M. (1972). Generalized Linear Models.

19. Pho, G.N., Goard, M.J., Woodson, J., Crawford, B., and Sur, M. (2018). Task-dependent representations of stimulus and choice in mouse parietal cortex. Nature Communications 2018 9:1 *9*, 1–16.

20. Chen, L.L., Lin, L.H., Green, E.J., Barnes, C.A., and McNaughton, B.L. (1994). Head-direction cells in the rat posterior cortex. I. Anatomical distribution and behavioral modulation. Exp Brain Res *101*, 8–23.

21. Nitz, D.A. (2012). Spaces within spaces: rat parietal cortex neurons register position across three reference frames. Nature Neuroscience 2012 15:10 *15*, 1365–1367.

22. Li, B., Nguyen, T.P., Ma, C., and Dan, Y. (2020). Inhibition of impulsive action by projection-defined prefrontal pyramidal neurons. Proc Natl Acad Sci U S A *117*, 17278–17287.

23. Kuan, A.T., Bondanelli, G., Driscoll, L.N., Han, J., Kim, M., Hildebrand, D.G.C., Graham, B.J., Wilson, D.E., Thomas, L.A., Panzeri, S., et al. (2024). Synaptic wiring motifs in posterior parietal cortex support decision-making. Nature 2024 627:8003 *627*, 367–373..

24. Cui, H., and Andersen, R.A. (2007). Posterior parietal cortex encodes autonomously selected motor plans. Neuron *56*, 552–559.

25. Crammond, D.J., and Kalaska, J.F. (2000). Prior information in motor and premotor cortex: activity during the delay period and effect on pre-movement activity. J Neurophysiol *84*, 986–1005.

26. Churchland, M.M., Yu, B.M., Ryu, S.I., Santhanam, G., and Shenoy, K. V. (2006). Neural Variability in Premotor Cortex Provides a Signature of Motor Preparation. Journal of Neuroscience *26*, 3697–3712.

27. Pesaran, B., Pezaris, J.S., Sahani, M., Mitra, P.P., and Andersen, R.A. (2002). Temporal structure in neuronal activity during working memory in macaque parietal cortex. Nature Neuroscience 2002 5:8 *5*, 805–811.

28. Gottlieb, J.P., Kusunoki, M., and Goldberg, M.E. (1998). The representation of visual salience in monkey parietal cortex. Nature 1998 391:6666 *391*, 481–484.

29. Hulsey, D., Zumwalt, K., Mazzucato, L., McCormick, D.A., and Jaramillo, S. (2024). Decision-making dynamics are predicted by arousal and uninstructed movements. Cell Rep *43*, 113709.

30. Reynolds, J.H., and Chelazzi, L. (2004). Attentional modulation of visual processing. Annu Rev Neurosci *27*, 611–647.

31. Ito, M., and Gilbert, C.D. (1999). Attention Modulates Contextual Influences in the Primary Visual Cortex of Alert Monkeys. Neuron *22*, 593–604.

32. McAdams, C.J., and Maunsell, J.H.R. (2000). Attention to both space and feature modulates neuronal responses in macaque area V4. J Neurophysiol *83*, 1751–1755.

33. Herrington, T.M., and Assad, J.A. (2010). Temporal sequence of attentional modulation in the lateral intraparietal area and middle temporal area during rapid covert shifts of attention. J Neurosci *30*, 3287–3296.

34. Cossell, L., Iacaruso, M.F., Muir, D.R., Houlton, R., Sader, E.N., Ko, H., Hofer, S.B., and Mrsic-Flogel, T.D. (2015). Functional organization of excitatory synaptic strength in primary visual cortex. Nature 2015 518:7539 *518*, 399–403.

35. Wilson, D.E., Scholl, B., and Fitzpatrick, D. (2018). Differential tuning of excitation and inhibition shapes direction selectivity in ferret visual cortex. Nature *560*, 97–101.

36. Herrington, T.M., Masse, N.Y., Hachmeh, K.J., Smith, J.E.T., Assad, J.A., and Cook, E.P. (2009). The effect of microsaccades on the correlation between neural activity and behavior in middle temporal, ventral intraparietal, and lateral intraparietal areas. J Neurosci *29*, 5793–5805.

37. Chen, S., Liu, Y., Wang, Z.A., Colonell, J., Liu, L.D., Hou, H., Tien, N.W., Wang, T., Harris, T., Druckmann, S., et al. (2024). Brain-wide neural activity underlying memory-guided movement. Cell *187*, 676-691.e16.

38. Steinmetz, N.A., Zatka-Haas, P., Carandini, M., and Harris, K.D. (2019). Distributed coding of choice, action and engagement across the mouse brain. Nature 2019 576:7786 *576*, 266–273.

39. Steinmetz, N.A., Aydin, C., Lebedeva, A., Okun, M., Pachitariu, M., Bauza, M., Beau, M., Bhagat, J., Böhm, C., Broux, M., et al. (2021). Neuropixels 2.0: A miniaturized high-density probe for stable, long-term brain recordings. Science (1979) *372*.

40. Chen, H., Chen, S., and Deng, X. (2019). A Universal Nonparametric Event Detection Framework for Neuropixels Data. bioRxiv, 650671.

41. Stine, G.M., Trautmann, E.M., Jeurissen, D., and Shadlen, M.N. (2023). A neural mechanism for terminating decisions. Neuron *111*, 2601-2613.e5.

42. Aleman, A., Hijman, R., De Haan, E.H.F., and Kahn, R.S. (1999). Memory impairment in schizophrenia: A meta-analysis. American Journal of Psychiatry *156*, 1358–1366.

43. Cellard, C., Tremblay, S., Lehoux, C., and Roy, M.A. (2007). Processing spatial–temporal information in recent-onset schizophrenia: The study of short-term memory and its susceptibility to distraction. Brain Cogn *64*, 201–207.

44. Guo, J.Y., Ragland, J.D., and Carter, C.S. (2018). Memory and cognition in schizophrenia. Molecular Psychiatry 2018 24:5 *24*, 633–642.

45. Moses, M., Tiego, J., Demontis, D., Bragi Walters, G., Stefansson, H., Stefansson, K., Børglum, A.D., Arnatkeviciute, A., and Bellgrove, M.A. (2022). Working memory and reaction time variability mediate the relationship between polygenic risk and ADHD traits in a general population sample. Molecular Psychiatry 2022 27:12 *27*, 5028–5037.

46. Pnevmatikakis, E.A., and Giovannucci, A. (2017). NoRMCorre: An online algorithm for piecewise rigid motion correction of calcium imaging data. J Neurosci Methods *291*, 83–94.

47. Digital Image Processing Using Matlab (Gonzalez) (2011).

48. Li, N., Daie, K., Svoboda, K., and Druckmann, S. (2016). Robust neuronal dynamics in premotor cortex during motor planning. Nature *532*, 459–464.

49. Finkelstein, A., Fontolan, L., Economo, M.N., Li, N., Romani, S., and Svoboda, K. (2021). Attractor dynamics gate cortical information flow during decision-making. Nat Neurosci *24*, 843–850.

50. Chadwick, A., Khan, A.G., Poort, J., Blot, A., Hofer, S.B., Mrsic-Flogel, T.D., and Sahani, M. (2023). Learning shapes cortical dynamics to enhance integration of relevant sensory input. Neuron *111*, 106-120.e10.